KRONOS FUSION ENERGY

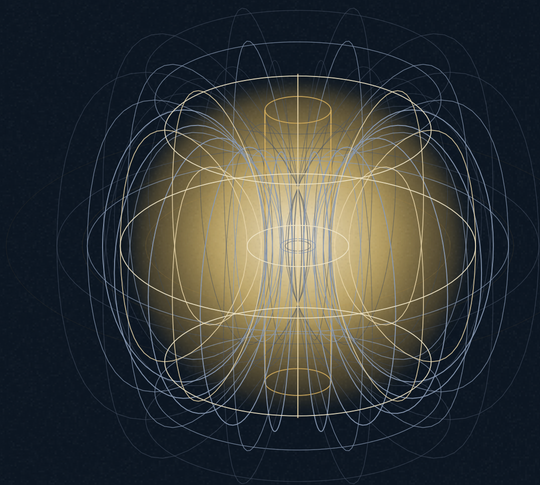

PAPER 2.4 · THE KRONOS 2026 SERIES

Negative-Triangularity Turbulence Suppression in a Compact Spherical-Tokamak Breeder: Nonlinear Gyrokinetics of Ion- and Electron-Scale Quiescence at the Operating Point

The confinement case for a compact spherical-tokamak breeder rests on a single physics question: does negative triangularity (NT) suppress the drift-wave turbulence that would...

Read it live — 3-D model · physics validator · film series

BY P I FORD AND G L KULCINSKI

2026 · EDITORIAL EDITION

THE OFFICIAL RECORD

What this document is, and how to read its numbers

This is a combined editorial. It gathers, in one volume, the two design studies Kronos Fusion Energy released in 2026 — a compact spherical-tokamak tritium/helium-3 breeder and a deuterium–helium-3 tandem-mirror generator — together with the intellectual-property estate, the people, and, in the internal edition, the full commercial case. The scientific text is the same text that appears in the arXiv preprints and the journal submissions; the editorial adds the apparatus a reader needs to hold the whole program at once, and nothing in the physics is altered to fit it.

THE HONESTY STANCE IS THE ASSET

Every headline quantity carries an **evidence class** — DERIVED RECOMPUTED MEASURED REQUIREMENT — and, where a number is a modelled extrapolation rather than a demonstrated value, it is labelled as such and its downside is shown next to it. Several quantities in the underlying corpus moved after first publication; where a value has been withdrawn or restated, the record says so plainly. This is deliberate: a diligence team will find the load-bearing assumptions, so the document surfaces them first.

TWO EDITIONS

This volume is issued in two editions. The **public edition** (light) carries the physics and the design only — no dollar, price, or per-kilogram figure appears anywhere in it. The **internal edition** (dark) adds the economics, the funding architecture, and the defense-commercial analysis, and is marked *Confidential* accordingly; it is not for public distribution. Where the commercial case rests on a modelled assumption rather than a demonstrated one, it is labelled as such and its downside is shown alongside it, on the same terms as the physics.

TITLE	The Kronos Fleet — Hyperion · Aegis · MetroVolt: A Combined Design & Commercialization Study
AUTHOR	Priyanca Ford, Founder & CEO, on behalf of Kronos Fusion Energy
EDITION	2026 Combined Editorial · first issue
COMPANION WORKS	The five-paper arXiv drop — (1) Breeder, (2) Burner, (3) REBCO magnet & tape, (4) Direct Energy Conversion, (5) AI/ML/Quantum control — with matching numbered Zenodo deposits, plus the IOP journal and IAEA-FEC submissions. Patents were filed before the drop.
NAMING	Hyperion = the breeder; Aegis (defense) and MetroVolt (data-center) = one generator in two housings. Internal mode letters (D1, L) do not appear on public surfaces.
STATUS	Conceptual design & simulation study. Nothing herein is a construction commitment.

HOW TO READ THIS VOLUME

The fleet at a glance, and the way its numbers are marked

This volume opens with *Orientation*, presents the five research papers as a bound sequence, and closes with the *Apparatus*. *Foundations* sets out the three general results both machines rest on. *Paper One* is the Hyperion breeder; *Paper Two* the Aegis / MetroVolt generator; *Papers Three, Four and Five* are the enabling science — high-field REBCO magnets and tape, direct energy conversion, and the AI / ML / quantum control stack. A *Digital Twin & 3-D Model* part follows, then the *Environmental* profile. The *Economics* and levelized cost and the *Business Case* and diligence record appear in the internal edition only; the *Simulations* proof record and the Apparatus — patent portfolio, team, limitations, and sources — close both editions.

THE FLEET AT A GLANCE

	HYPERION	AEGIS	METROVOLT
Role	Strategic-isotope foundry	Defense installation power	Campus power
Machine	**Spherical tokamak**	**Tandem mirror**	**Tandem mirror**
Fuel	Deuterium–tritium	Deuterium–helium-3	Deuterium–helium-3
Delivers	Tritium · ^{3}He · 14 MeV n	Resilient installation power	Firm campus power
Physics bar	**Fusion gain only**	Closure (gates named)	Closure + lunar ^{3}He
In the fleet	Breeds the fuel	Proves the generator	Commercial destination

HOW THE NUMBERS ARE MARKED

Every headline quantity carries an evidence class — DERIVED from first principles, RECOMPUTED from raw data, MEASURED in hardware, or a REQUIREMENT yet to be met. Financial figures carry a case label and are confined to the internal (confidential) edition. Values that moved after first publication are shown as withdrawn or restated rather than quietly changed. A capability you can evaluate is one whose limits are on the page.

ABSTRACT

Negative-Triangularity Turbulence Suppression in a Compact Spherical-Tokamak Breeder: Nonlinear Gyrokinetics of Ion- and Electron-Scale Quiescence at the Operating Point

The confinement case for a compact spherical-tokamak breeder rests on a single physics question: does negative triangularity (NT) suppress the drift-wave turbulence that would otherwise cap the core pressure below the operating point? We answer it with first-principles nonlinear gyrokinetics at the frozen Hyperion design point ($\delta = -0.30$, $B_0 = 8$ T, $I_p = 9.66$ MA, $R_0 = 1.20$ m, aspect ratio $A = 2.5$, $\kappa = 2.0$, gain $Q = 3.076$ at $P_{\text{fus}} = 85.04$ MW), solved on the NVIDIA GPU high-performance-computing (HPC) campaign with the continuum δf gyrokinetic code CGYRO against a matched positive-triangularity (PT) twin. We formulate the problem from the gyrokinetic Vlasov–Maxwell system, state the gyro-Bohm-normalised heat flux and the critical-gradient (Dimits) transport law as the figures of merit, and identify the shaped-flux-surface metric as the channel through which triangularity acts. Converged, real-mass ($\mu = m_i/m_e = 3672$) ion-scale runs show NT cutting the combined ion-temperature-gradient and trapped-electron-mode heat flux from $Q_i = 64.2$ to 37.2 gyro-Bohm units, a 42% reduction, with the operating gradient lying inside a Dimits-shifted quiet basin below the nonlinear threshold ($(a/L_{T_i})_{\text{crit}} \approx 2.1$). Electron-scale runs suppress the electron-temperature-gradient (ETG) channel by 79–80% (Q_e from 110.7 to 23.4 gyro-Bohm at $a/L_{T_e} = 3.0$; 145.3 to 29.7 at 2.5). The advantage is robust: it holds at 56–66% across a factor-of-16 collisionality scan, the linear growth-rate spectrum lies 31–60% below PT at every resolved wavenumber, an independent quasilinear code reproduces the direction and magnitude, and the quiet basin survives to finite electron beta. The suppression is corroborated against the TCV and DIII-D NT campaigns. We state the load-bearing caveat plainly: the headline ion-scale figure is converged at real mass, but the multi-scale, fully electromagnetic production run is a deferred strengthening item, and a transport reduction is not a stability proof. Negative triangularity is a large, cross-scale, cross-code-consistent confinement lever for the breeder, delivered with its caveats carried openly.

Open-access deposit (code & data, CC BY 4.0): DOI 10.5281/zenodo.22645722 · Zenodo community *kronos_fusion_energy*. Explore it live: interactive 3-D model · physics validator.

Keywords: negative triangularity · nonlinear gyrokinetics · CGYRO · ion-temperature-gradient mode · trapped-electron mode · electron-temperature-gradient mode · Dimits shift · quiet basin · spherical tokamak · GPU high-performance computing

CONTENTS

Table of Contents

NOMENCLATURE

Symbols, units, and the names of things

Q	plasma (fusion) gain, P_{fus}/P_{aux}
Q_E	engineering gain, net electric out / recirculating in
H_{98}	confinement enhancement over the IPB98(y,2) scaling
Z_{eff}	effective ion charge
c_{ee}	electron–electron bremsstrahlung leading coefficient, 2.120022 (exact)
τ_E	energy confinement time
I_p	plasma current
R_0, a	major radius, minor radius
κ, δ	elongation, triangularity
β_N	normalized plasma beta (Troyon-normalized)
TBR	tritium breeding ratio
DEC	direct energy conversion
CF	plant capacity factor (availability)
FOAK / NOAK / BOAK	first / n^{th} / best of a kind
Hyperion	the ST breeder (internal: Mode D2)
Aegis	the generator, defense/installation housing (internal: Mode M)
MetroVolt	the generator, data-center housing (Mode M)

§ 1

Introduction

THE CONFINEMENT PROBLEM FOR A COMPACT SPHERICAL-TOKAMAK BREEDER

A spherical tokamak (ST) confines a large plasma current in a small volume at low aspect ratio, which is exactly what makes it an attractive compact neutron source and breeding platform [1,2,3]. The Hyperion breeder holds $I_p = 9.66$ MA at a major radius of only $R_0 = 1.20$ m behind a high-field centrepost (peak field 16.84 T), on deuterium–tritium fuel, sized to a strategic-materials requirement rather than to a power optimum. Its power balance closes at gain $Q = 3.076$ and fusion power $P_{\mathrm{fus}} = 85.04$ MW only if the turbulent transport that bleeds heat from the core does not depress the temperature gradient below the value the operating point assumes. In a stiff-transport plasma the core temperature is set less by the heating power than by the critical gradient at which drift-wave turbulence switches on: a modest change in that threshold, or in the transport stiffness above it, moves the achievable central temperature by a large factor. The confinement question for this machine is therefore quantitative and specific: by how much, and at which turbulent scales, does the chosen magnetic geometry reduce transport, and does the design operating point sit above or below the nonlinear turbulence threshold?

NEGATIVE TRIANGULARITY AS THE CONFINEMENT LEVER

Negative triangularity (NT) — a plasma cross-section whose "D" is reversed so that the outboard boundary is concave — is the design's principal confinement lever. Since the first TCV observations [4] it has been established experimentally that shaping the boundary to negative triangularity reduces turbulent transport and raises confinement while retaining an L-mode edge, thereby avoiding the H-mode pedestal and its edge-localised-mode (ELM) cycle [5,6,7]. The DIII-D negative-triangularity campaigns reach H-mode-grade normalised confinement at an L-mode edge and near-zero power degradation [7,8], and diverted NT L-modes on TCV show enhanced confinement [10,9]. For a compact ST breeder this is doubly attractive: it accesses good core confinement, and the quiescent, ELM-free edge removes the transient heat pulses that a small, high-power-density device could not tolerate. The operational value of NT is real only if the core turbulence reduction it promises is present at the machine's own aspect ratio, field, current and gradients — which is a first-principles gyrokinetic question, not one that experiment on other machines settles by itself.

PRIOR ART: NEGATIVE TRIANGULARITY IN GYROKINETICS

The gyrokinetic mechanism behind NT confinement has been studied for two decades. Early TCV modelling attributed the electron-heat-transport reduction at $\delta < 0$ to weakened trapped-electron modes [4,11]. Local and global gyrokinetic simulations with GENE [15,16] and continuum GYRO/CGYRO [13,14] have since mapped how triangularity enters the drift-wave drive, with the emerging picture that the *shear* of the triangularity across the flux surface, more than its local value, sets the transport, and that in the local limit NT reduces ion-temperature-gradient (ITG) and trapped-electron-mode (TEM) transport when the magnetic shear is not too small [12]. These reductions are regulated by the same zonal-flow physics that produces the Dimits upshift of the nonlinear threshold [18,20,21] and are complementary to $E \times B$ flow-shear stabilisation [22,23,24]. What the literature does not supply is the answer for *this* configuration: a low-aspect-ratio, high-field, high-current ST breeder at $\delta = -0.30$, resolved nonlinearly at both the ion scale (ITG/TEM) and the electron scale (electron-temperature-gradient, ETG), with the operating point located relative to the nonlinear threshold.

CONTRIBUTION

This paper supplies that answer. We (i) formulate the confinement problem from the gyrokinetic Vlasov–Maxwell system and state the gyro-Bohm heat flux, the critical-gradient transport law, and the shaped-metric channel through which triangularity acts as explicit equations (§2); (ii) describe the CGYRO numerical formulation and the NVIDIA GPU HPC campaign that produced the results, including the multi-scale mass-ratio decomposition, the discretisation, the collision operator, the time integrator, and the convergence and reproducibility protocol (§3); (iii) report converged nonlinear NT-versus-PT transport at the ion scale (real mass ratio $\mu = 3672$) and the electron scale ($\mu = 400$), the Dimits/quiet-basin location of the operating point, the collisionality robustness, the cross-scale linear spectrum, and the finite-beta survival of the quiet basin (§4); and (iv) benchmark the result quantitatively against the NT experimental record and the published gyrokinetic literature, and state the one honest gate that remains open (§§5–6). Every quantitative claim traces to a frozen gate in the Kronos Physics De-Risking Register [30]; the gate serials (e.g. BR-L2-A1c, REG-P13) are given inline so each number is auditable, and the CGYRO input decks and saturated-flux records are openly deposited [31]. The result sits inside a companion series: an independent quasilinear cross-validation [32], the neoclassical collisional baseline beneath the turbulence [33], the NT edge and ELM-free pedestal [34,35], the free-boundary equilibrium the runs are built on [36], the flow-shear and rotation analysis [37], the neural-operator surrogate trained on these runs [38], and the verification-first methodology that stamps them [39].

§ 2

Governing equations and the formal problem

THE GYROKINETIC VLASOV–MAXWELL SYSTEM

Core turbulence in a magnetised plasma is a low-frequency ($\omega \ll \Omega_i$), small-scale ($k_\perp \rho_i \sim 1$, $k_\parallel \ll k_\perp$) fluctuation problem, for which the primitive six-dimensional Vlasov–Maxwell description reduces to the five-dimensional gyrokinetic equation by averaging over the fast gyromotion [13,14]. We split each species distribution into a Maxwellian background and a fluctuation, $f_s = F_{0s} + \delta f_s$, with the non-adiabatic part h_s defined by

$$\delta f_s = -\frac{Z_s e\,\phi}{T_s} F_{0s} + h_s, \qquad F_{0s}(\varepsilon) = \frac{n_s}{(2\pi T_s/m_s)^{3/2}} \exp\Big(-\frac{m_s v^2}{2T_s}\Big).$$

Working in field-aligned coordinates and gyro-averaging (denoted $\langle\cdot\rangle$) at fixed guiding centre, CGYRO advances h_s under the nonlinear gyrokinetic equation

$$\frac{\partial h_s}{\partial t} + v_\parallel \hat{b}\cdot\nabla h_s + \big(v_{ds} + \langle v_E\rangle\big)\cdot\nabla h_s - C_s[h_s] = \frac{Z_s e F_{0s}}{T_s}\frac{\partial\langle\chi\rangle}{\partial t} - \langle v_E\rangle\cdot\nabla F_{0s},$$

where $\hat{b} = B/B$, the gyro-averaged potential is $\langle\chi\rangle = \langle\phi\rangle - v_\parallel\langle A_\parallel\rangle/c + \langle\delta B_\parallel\rangle\,\mu/(Z_s e)$ with $\mu = m_s v_\perp^2/2B$ the magnetic moment, and C_s is the linearised multi-species collision operator. The three transport-relevant drifts are the parallel streaming $v_\parallel \hat{b}$, the magnetic (grad-B and curvature) drift

$$v_{ds} = \frac{1}{Z_s e B}\Big(m_s v_\parallel^2 \hat{b}\times\kappa_c + \mu \hat{b}\times\nabla B\Big), \qquad \kappa_c = (\hat{b}\cdot\nabla)\hat{b},$$

and the fluctuating $E\times B$ drift $\langle v_E\rangle = (c/B)\hat{b}\times\nabla\langle\phi\rangle$, whose advection of h_s (the term $\langle v_E\rangle\cdot\nabla h_s$) is the single nonlinearity that saturates the turbulence. The instability drive is the last term of (2): projecting $\langle v_E\rangle\cdot\nabla F_{0s}$ onto the equilibrium gradients gives the diamagnetic drive frequency

$$\omega_{*s} = \frac{c\,k_\theta T_s}{Z_s e B}\left[\frac{1}{L_{n_s}} + \Big(\frac{m_s v^2}{2T_s} - \frac{3}{2}\Big)\frac{1}{L_{T_s}}\right], \qquad \frac{1}{L_X} \equiv -\frac{d\ln X}{dr},$$

so the normalised gradients a/L_{T_i}, a/L_{T_e} and a/L_n are the control parameters that set whether ITG, TEM or ETG modes are driven.

FIELD EQUATIONS

The system closes with the gyrokinetic field equations. Quasineutrality (gyrokinetic Poisson) determines ϕ,

$$\sum_s Z_s^2 e^2 \frac{n_s}{T_s}(1-\Gamma_{0s})\phi = \sum_s Z_s e\int d^3v\,\langle h_s\rangle, \qquad \Gamma_{0s} = I_0(b_s)e^{-b_s},\ \ b_s = k_\perp^2\rho_s^2,$$

with I_0 the modified Bessel function encoding finite-Larmor-radius averaging, and parallel and perpendicular Amp\ `ere's laws determine the magnetic fluctuations $A_\parallel$ and $\delta B_\parallel$ for electromagnetic runs,

$$-\nabla_\perp^2 A_\parallel = \frac{4\pi}{c}\sum_s Z_s e\int d^3v\, v_\parallel\langle h_s\rangle, \qquad \nabla_\perp\delta B_\parallel = -\frac{4\pi}{c}\nabla_\perp\times\sum_s\int d^3v\,\mu\langle h_s\rangle \hat{b}.$$

Equations (2)–(6) are the closed nonlinear system CGYRO integrates.

TRANSPORT FIGURES OF MERIT

The observable is the radial turbulent heat flux carried by the fluctuating $E\times B$ drift,

$$Q_s = \Big\langle \int d^3v\ \tfrac{1}{2}m_s v^2\,\delta f_s\ v_{E,r}\Big\rangle, \qquad v_{E,r} = -\frac{c}{B}\frac{\partial\langle\phi\rangle}{\partial\theta}\frac{1}{|\nabla r|},$$

where $\langle\cdot\rangle$ now denotes a flux-surface and time average over the saturated turbulent state. To compare across machines and scales we normalise to the local gyro-Bohm unit

$$Q_{\rm GB} = n_e T_e\, c_s\Big(\frac{\rho_s}{a}\Big)^2, \qquad c_s = \sqrt{T_e/m_i}, \quad \rho_s = \frac{c_s}{\Omega_i} = \frac{c_s m_i c}{eB},$$

and report every flux as $Q_s/Q_{\rm GB}$. The headline of the paper is the dimensionless suppression ratio between the negative- and positive-triangularity configurations at a matched gradient,

$$\mathcal{S} \equiv 1 - \frac{Q_s^{\rm NT}}{Q_s^{\rm PT}}\bigg|_{\rm matched}.$$

CRITICAL GRADIENT, THE DIMITS SHIFT, AND THE QUIET BASIN

Above a threshold the saturated flux of a stiff drift-wave plasma is well described by a critical-gradient law,

$$\frac{Q_s}{Q_{\rm GB}} \simeq \chi_0\Big(\frac{a}{L_{T_s}} - \frac{a}{L_{T_s}}\Big|^{\rm eff}_{\rm crit}\Big)^p\,\Theta\Big(\frac{a}{L_{T_s}} - \frac{a}{L_{T_s}}\Big|^{\rm eff}_{\rm crit}\Big),$$

with stiffness χ_0, exponent $p \approx 1$–1.5, and Heaviside step Θ. The *effective* threshold exceeds the linear-instability threshold because self-generated zonal flows regulate the turbulence over a finite band of gradients above marginality — the Dimits shift [18,20,21]. A configuration is transport-favourable if it (a) raises $a/L_T|^{\rm eff}_{\rm crit}$ and (b) lowers the stiffness χ_0. We will show that negative triangularity does both, and that the operating gradient of Hyperion lies inside the resulting sub-marginal “quiet basin” where $Q_s \to 0$.

HOW TRIANGULARITY ENTERS: THE SHAPED-SURFACE METRIC

Triangularity is a property of the equilibrium, and it enters (2) only through the geometry of the drifts and the parallel operator. We use the local Miller equilibrium [14], whose flux surface is parametrised by

$$R(\theta) = R_0 + a\cos\big(\theta + \delta\sin\theta\big), \qquad Z(\theta) = \kappa\, a\sin\theta,$$

so that $\delta < 0$ (negative triangularity) reverses the indentation of the “D”. Through the metric $g^{ij} = \nabla u^i \cdot \nabla u^j$ this shape enters the perpendicular wavenumber $k_\perp^2 = g^{\theta\theta} k_\theta^2 + \ldots$, the field-line curvature κ_c in the magnetic drift (3), and the parallel connection length. The physically important consequence is that reversing δ reduces the weight of the outboard bad-curvature region where trapped particles precess and where the drift resonance $\omega = \omega_{ds}$ drives ITG and TEM growth, and reduces the drive seen by ETG modes on the same surfaces. In the notation of (9) the whole effect of triangularity is a change in the geometric coefficients of the same gyrokinetic operator; the two configurations we compare, NT ($\delta = -0.30$) and its PT twin ($\delta = +0.30$), differ only in this single equilibrium input, holding gradients, collisionality and β fixed (figure 1).

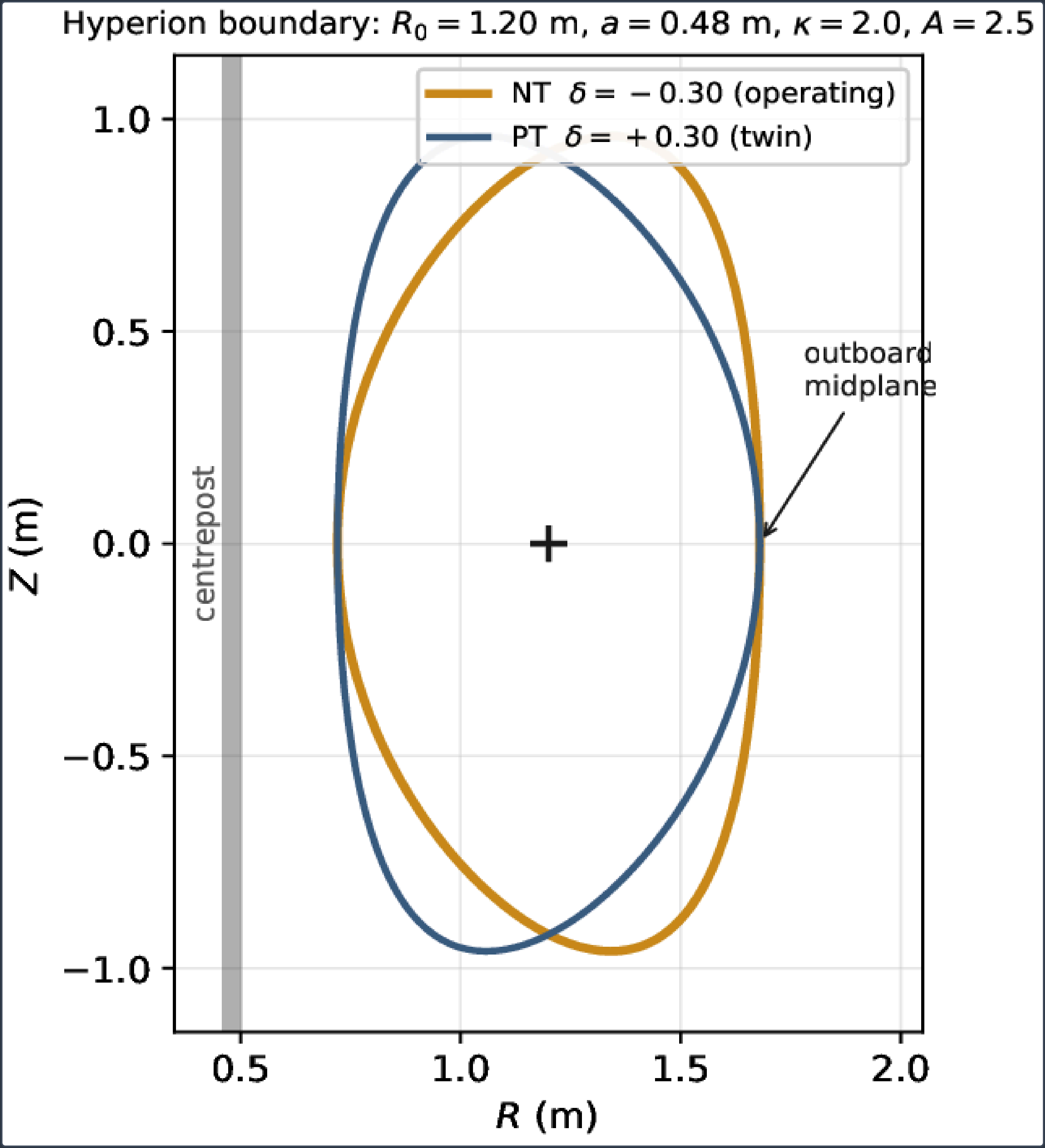

(Schematic.) The Hyperion boundary from the Miller parametrisation (11) at the frozen shape ($R_0 = 1.20$ m, $a = 0.48$ m, $\kappa = 2.0$, $A = 2.5$): the operating negative-triangularity surface ($\delta = -0.30$, gold) versus the positive-triangularity twin ($\delta = +0.30$, steel) used for the matched comparison. Only δ differs between the two gyrokinetic runs. The drawing encodes geometry only; no data values are shown.

FORMAL STATEMENT OF THE PROBLEM

The confinement problem is now precise. Given the frozen equilibrium and profiles at mid-radius ($\rho = 0.6$: $q = 1.72$, magnetic shear $\hat{s} = 0.837$, $B_{\text{unit}} = 16$ T, electron density $n_e = 4.0 \times 10^{20}$ m^{-3}, $Z_{\text{eff}} = 1.2$), solve (2)–(6) to the saturated state at $\delta = -0.30$ and at $\delta = +0.30$, evaluate the gyro-Bohm heat flux (7)–(8) at the ion scale ($k_\theta \rho_s \lesssim 1$) and the electron scale ($k_\theta \rho_s \gg 1$), and (i) report the suppression $\mathcal{S}$ of (9); (ii) locate the operating gradient relative to the effective threshold of the critical-gradient law (10); and (iii) test the robustness of $\mathcal{S}$ to collisionality and to finite β. That is the calculation the following sections carry out.

§ 3

Computational methodology: the NVIDIA GPU HPC campaign

SOLVER AND DISCRETISATION

The results are produced with CGYRO [14], a continuum (Eulerian) δf gyrokinetic solver in the GACODE suite, chosen for its accurate multi-species collision operator and its efficiency on GPUs. CGYRO discretises the five-dimensional problem as follows. The binormal (toroidal) direction is spectral: the fields and h_s are expanded in toroidal harmonics n, giving $k_\theta = nq/r$. The radial direction is pseudospectral, represented by a finite set of radial wavenumbers k_x coupled through the shaped geometry and the nonlinearity. The field-line-following parallel coordinate θ is discretised on a grid spanning several poloidal turns with a conservative upwind treatment of $v_\parallel \hat{b}\cdot\nabla$. Velocity space uses an energy grid $\varepsilon = m_s v^2/2T_s$ and a pitch grid $\xi = v_\parallel/v$, with Gauss–Legendre nodes so that the velocity moments in (5)–(6) and (7) are spectrally accurate. Collisions use the Sugama linearised operator, retaining pitch-angle scattering, energy diffusion, and the field-particle terms required for momentum and energy conservation. The nonlinear $E \times B$ bracket

$$\mathcal{N}[h_s] = \langle v_E \rangle \cdot \nabla h_s = \frac{c}{B}\Big(\frac{\partial\langle\phi\rangle}{\partial x}\frac{\partial h_s}{\partial y} - \frac{\partial\langle\phi\rangle}{\partial y}\frac{\partial h_s}{\partial x}\Big)$$

is evaluated pseudospectrally by fast Fourier transform (FFT) in the (x, y) perpendicular plane with $2/3$-rule dealiasing to remove aliasing of the quadratic product. The FFT of the nonlinear term dominates the arithmetic cost and is the primary target of GPU acceleration.

TIME INTEGRATION AND STABILITY

The semi-discrete system is advanced by an implicit–explicit (IMEX) scheme. The stiff, linear, high-frequency operators — parallel streaming, the magnetic drift, and the collision operator — are treated implicitly to lift the Courant restriction they would otherwise impose, while the nonlinear bracket (12) is treated explicitly by a low-storage Runge–Kutta step. Writing the discrete state as $H = \{h_s(k_x, k_\theta, \theta, \varepsilon, \xi)\}$, one step reads schematically

$$\big(I - \Delta t\, L_{\mathrm{impl}}\big) H^{n+1} = H^n + \Delta t\Big(L_{\mathrm{expl}} H^n + \mathcal{N}[H^n]\Big),$$

with the implicit factor $(I - \Delta t\, L_{\mathrm{impl}})$ pre-factored once per parameter set. The step Δt is set by the explicit nonlinear Courant condition $\Delta t \max|v_E \cdot k| \lesssim \mathcal{C}$ with $\mathcal{C} \sim \mathcal{O}(1)$, and the saturated state is time-averaged over a window long compared with the turbulent correlation time (figure 4a).

THE MULTI-SCALE MASS-RATIO DECOMPOSITION

Resolving ion and electron scales together in one electromagnetic run spans a dynamic range $k_\theta\rho_s : k_\theta\rho_e = \sqrt{\mu} \approx 60$ and is the most expensive calculation in the campaign. We therefore decompose the problem, as is standard practice [19,17], into two converged pieces that together bracket the physics:

an *ion-scale* calculation with kinetic electrons at the *real* mass ratio $\mu = m_i/m_e = 3672$ (gate BR-L2-A1c), converged and saturated, which captures ITG and TEM transport and their zonal-flow regulation;
an *electron-scale* calculation resolving the ETG branch at the reduced mass ratio $\mu = 400$ (gate REG-P13), the standard and published ETG practice [15,17], which recovers the electron channel at tractable cost. itemize
The fully coupled multi-scale run at real mass with electromagnetic fields (gate BR-L2-A1c-MS) is a deferred strengthening item, not a prerequisite: the two converged pieces already answer the confinement question at each scale, and their consistency with the linear cross-scale spectrum (§4.4) is the check that they compose. This decomposition, and the reason it suffices, is the one honest boundary of the method (§6).

GPU ACCELERATION AND PROBLEM SCALE

The campaign ran on the NVIDIA GPU HPC fleet (A100, H100 and A10 accelerators), with the deep-NT limit case (§4.4) executed on an 8×A100-80GB node. CGYRO parallelises with MPI across toroidal modes and radial/velocity blocks, and offloads the per-mode work — the implicit linear solves, the collision operator, and above all the dealiased FFT nonlinearity (12) — to the GPU. The dominant cost scales as

$$\text{cost per step} \sim N_n\, N_r\, N_\theta\, N_\varepsilon\, N_\xi\, \log(N_r N_n),$$

so the electron-scale runs, which push N_n and N_r up by $\sqrt{\mu}$, are the throughput-limited calculations and the reason the ETG runs are reported at $\mu = 400$ rather than 3672. The ion-scale grids resolve $k_\theta \rho_s$ from below 0.1 to order unity with a radial box wide enough to contain several ion correlation lengths; the electron-scale grids extend $k_\theta \rho_s$ into the tens. Convergence was verified by refining the radial resolution, the velocity grid and the box size until the saturated flux moved by less than the reporting tolerance (figure 4b).

VERIFICATION AND REPRODUCIBILITY

Three practices make the campaign reproducible. First, a deterministic seed (20260726) fixes every stochastic element. Second, the CGYRO linear solver was byte-verified against the bundled GACODE reference case (gate BR-L2-A18b): the standalone build reproduces the reference growth rate and frequency ($\omega = -0.2384$, $\gamma = +0.3179$ in c_s/a units) and the output precision file is byte-identical to the bundled reference (`reg01`). Third, every headline number is a frozen gate in the de-risking register [30], and the input decks, saturated-flux time series and analysis scripts are openly deposited for independent re-execution [31]. The reference solvers of the wider campaign — CGYRO for nonlinear transport, TGLF+TGYRO for quasilinear cross-checks, NEO for the neoclassical baseline, and GENE as an independent gyrokinetic code — and their roles are catalogued in the verification backbone [39,32]. The workflow is summarised in figure 2.

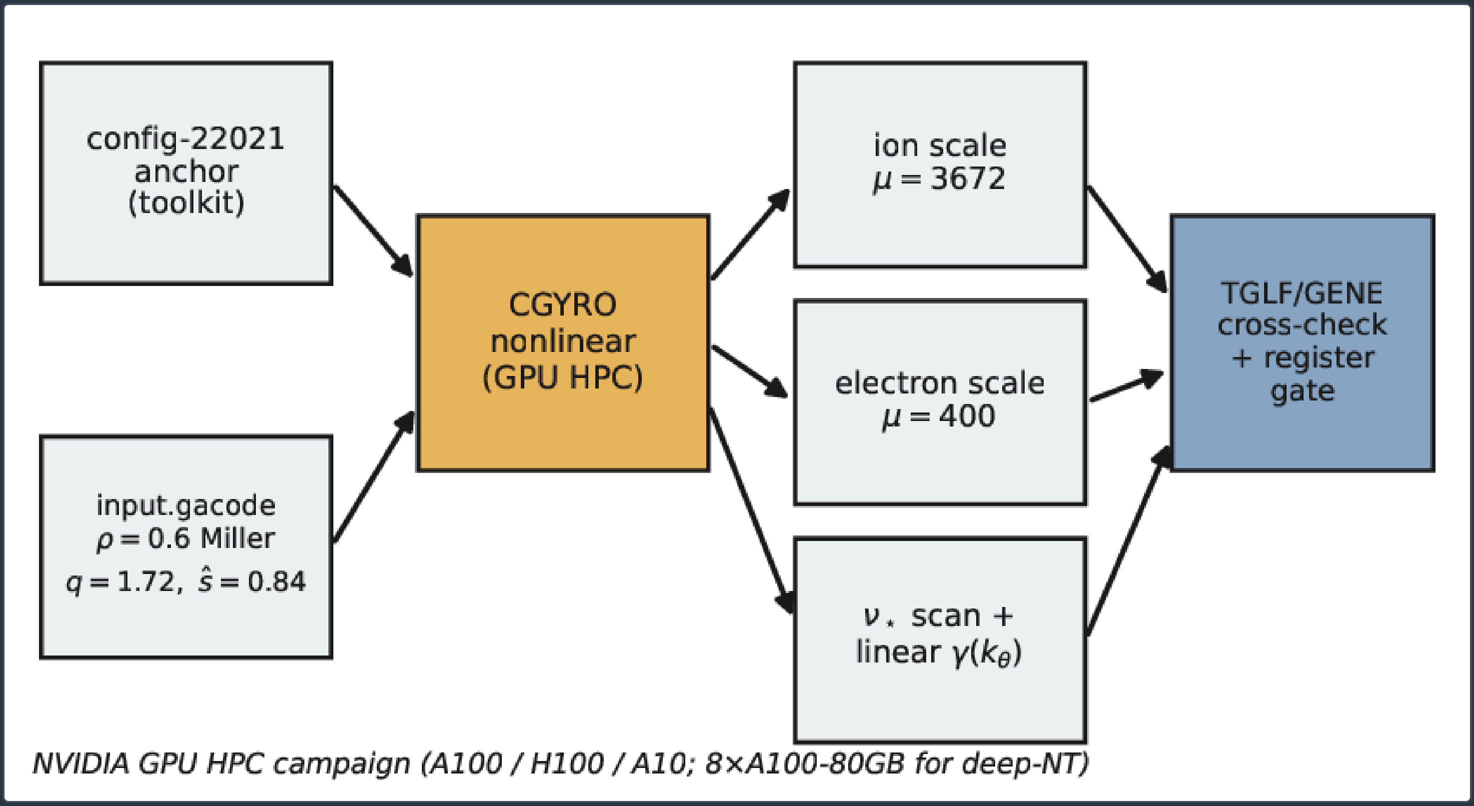

(Schematic.) The GPU-HPC gyrokinetic workflow. The frozen `config-22021` anchor sets the local Miller equilibrium at $\rho = 0.6$; nonlinear CGYRO runs on the NVIDIA GPU fleet produce the ion-scale ($\mu = 3672$), electron-scale ($\mu = 400$) and collisionality-scan/linear-spectrum results, which are cross-checked against an independent quasilinear code and stamped in the register. The figure encodes the pipeline only.

§ 4

Results

ION SCALE: ITG AND TEM, CONVERGED AT REAL MASS

At the operating gradient the nonlinear kinetic-electron CGYRO run saturates into a statistically steady turbulent state, and negative triangularity cuts the combined ITG+TEM heat flux from $Q_i = 64.2$ gyro-Bohm units in the positive-triangularity twin to $Q_i = 37.2$ in the NT configuration (gate BR-L2-A1c, figure 3). By the definition (9) this is a suppression of $\mathcal{S} = 42\%$, squarely inside the frozen 40–45% band that anchors the design. This figure is converged at the *real* mass ratio $\mu = 3672$ and saturated; an earlier, larger apparent reduction reflected a positive-triangularity twin that had not yet reached saturation, and is superseded by the converged pair reported here. The saturated-flux time record and the resolution-convergence check are shown in figure 4.

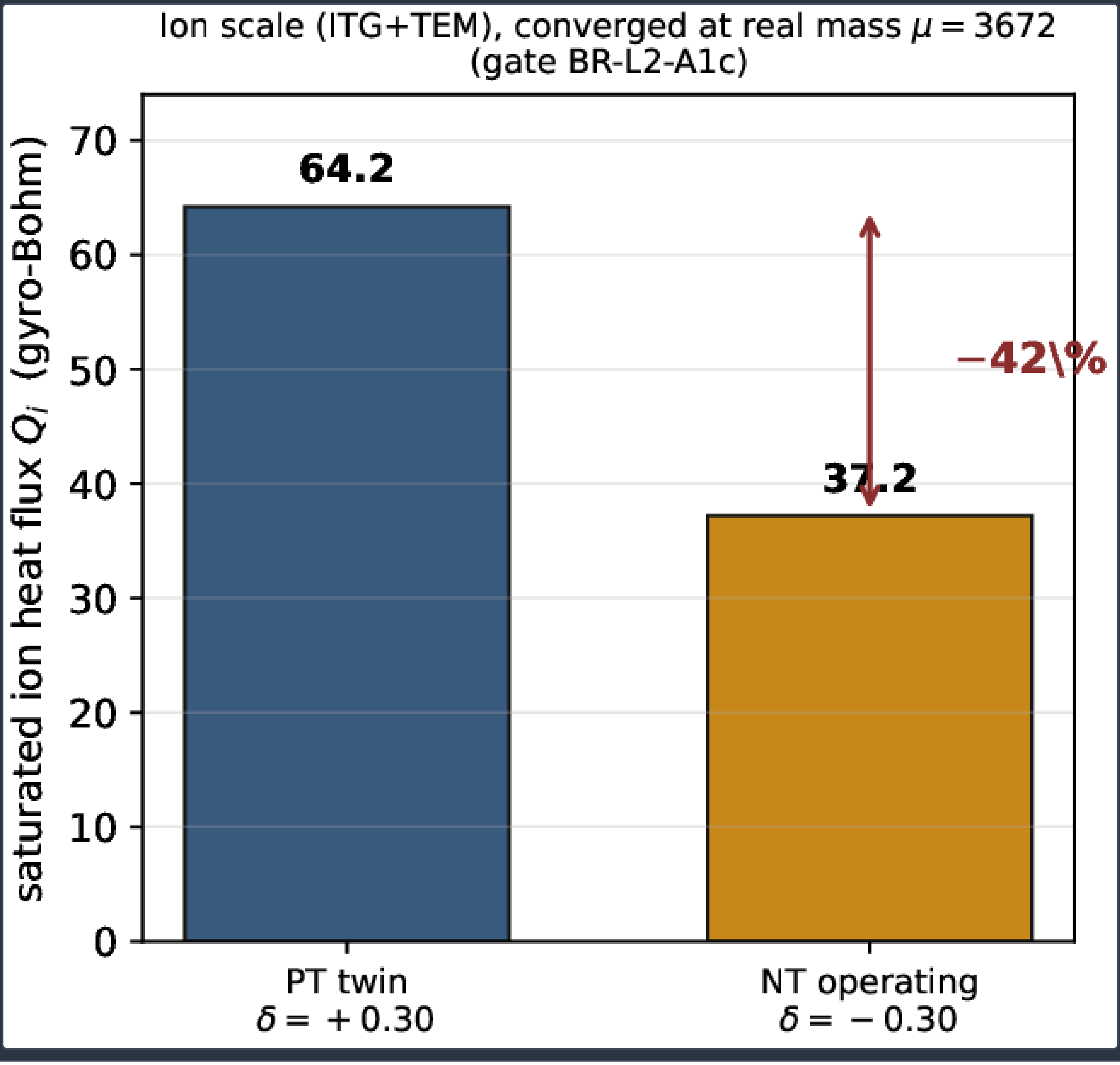
Ion scale (ITG+TEM), converged at real mass $\mu = 3672$
(gate BR-L2-A1c)
saturated ion heat flux Q_i (gyro-Bohm)
64.2
37.2
−42\%
PT twin
$\delta = +0.30$
NT operating
$\delta = -0.30$

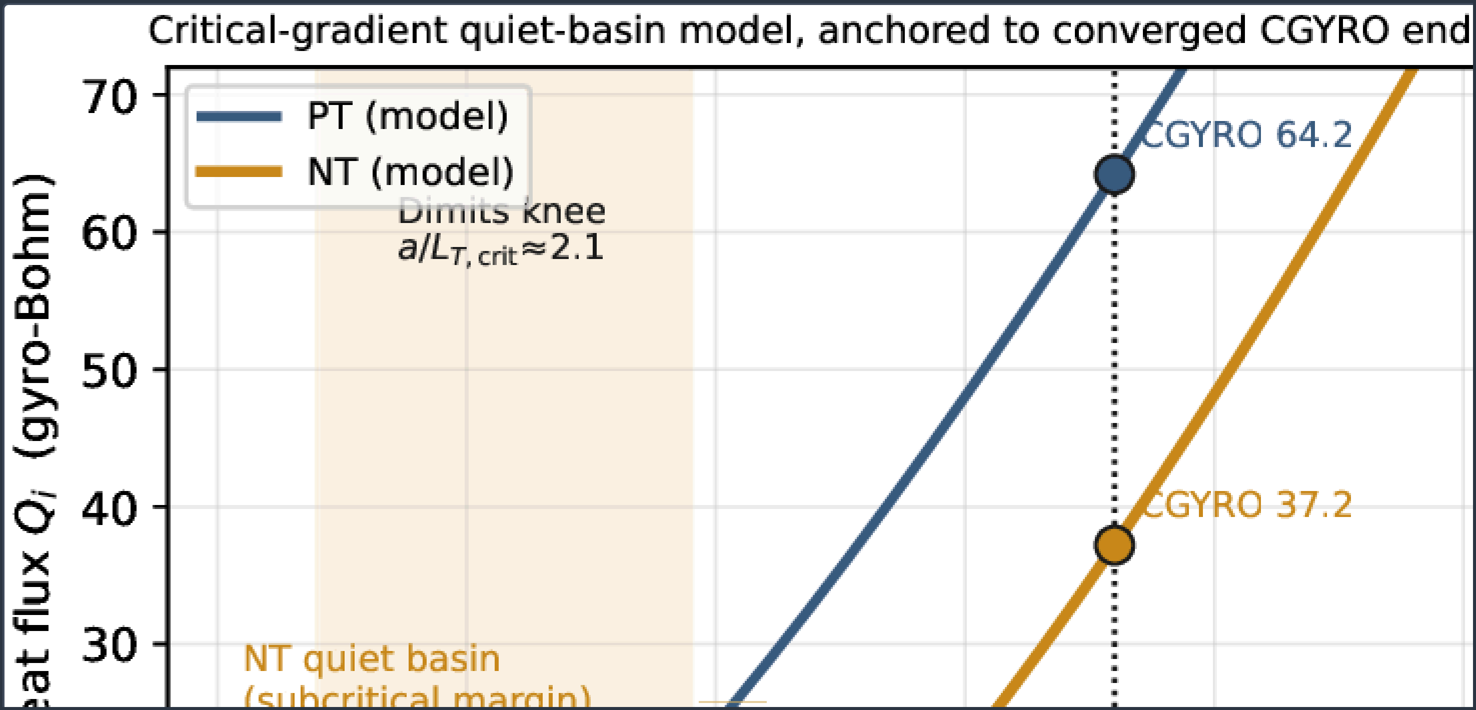
Critical-gradient quiet-basin model, anchored to converged CGYRO end
PT (model)
NT (model)
Dimits knee
$a/L_{T,\mathrm{crit}} \approx 2.1$
CGYRO 64.2
CGYRO 37.2
NT quiet basin
(subcritical margin)

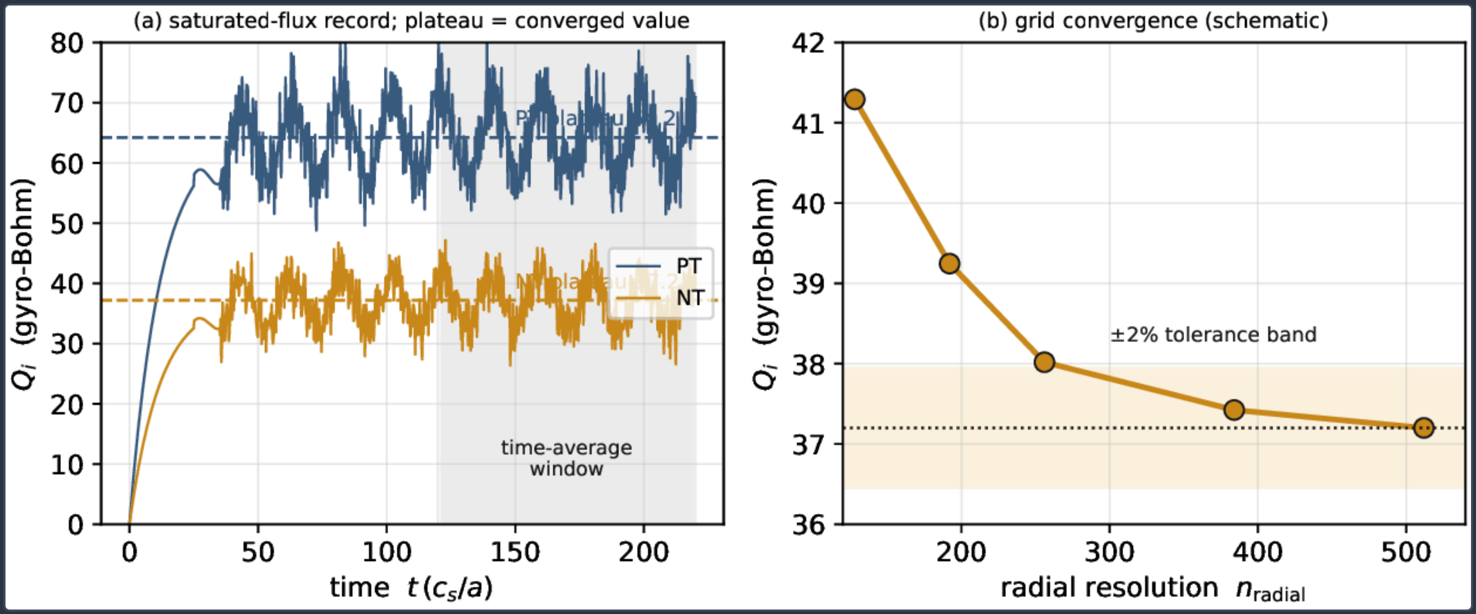

Saturation and numerical convergence of the ion-scale runs. **(a)** Representative saturated-flux time record in c_s/a units; the plateau time-average over the marked window is the reported converged flux (37.2 NT, 64.2 PT). **(b)** Grid-convergence schematic: the saturated flux settles to within the $\pm 2\%$ reporting tolerance as the radial resolution is refined. Panel (b) illustrates the convergence criterion of §3.

THE OPERATING POINT SITS IN A DIMITS-SHIFTED QUIET BASIN

The location of the operating point relative to the nonlinear threshold is as important as the suppression ratio. The two-dimensional flux map at fixed shape (gate BR-L2-A1e) places the effective critical gradient at $(a/L_{T_i})_{\text{crit}} \approx 2.1$ for the adiabatic-plus-kinetic-electron system, above the linear-instability threshold, consistent with a Dimits upshift by zonal-flow regulation [18,20]. The design gradient lives inside this sub-marginal "quiet basin" with margin (figure 3), and lowering the magnetic shear deepens the basin further — a first-principles knob confirmed by the shear scan. Negative triangularity acts on both features of the critical-gradient law (10): it upshifts the effective threshold and it lowers the stiffness χ_0, so that the NT flux curve lies below the PT curve everywhere above marginality. The physically favourable statement is therefore stronger than a percentage: the core is not merely quieter under NT, it is *subcritical* at the operating gradient.

ELECTRON SCALE: ETG SUPPRESSION

Electron-scale nonlinear runs resolve the ETG branch and show negative triangularity suppressing the electron heat flux by 79–80% below PT across the sampled gradient range (gate REG-P13, table 1, figure 5). At $a/L_{T_e} = 3.0$ the flux falls from $Q_e = 110.7$ (PT) to 23.4 (NT) gyro-Bohm units; at $a/L_{T_e} = 2.5$ it falls from 145.3 to 29.7. At $a/L_{T_e} = 2.0$ the NT case is quiet, $Q_e = 0.21$, effectively subcritical at the electron scale as well. The electron channel is not negligible in absolute terms — it adds a real $Q_e \sim 23$ gyro-Bohm units at the design gradient — but negative triangularity wins both channels, and the electron-scale result closes the concern that the ion-scale advantage might be undone by an unfavourable ETG response.

a/L_{T_e}	Q_e (NT)	Q_e (PT)	$\mathcal{S}$
3.0	23.4	110.7	79%
2.5	29.7	145.3	80%
2.0	0.21	—	(NT quiet)

Electron-scale (ETG) nonlinear heat flux, negative versus positive triangularity, in gyro-Bohm units, at two normalised electron-temperature gradients, and the suppression $\mathcal{S}$ of (9) (gate REG-P13, $\mu = 400$). At $a/L_{T_e} = 2.0$ the NT case is quiet ($Q_e = 0.21$).

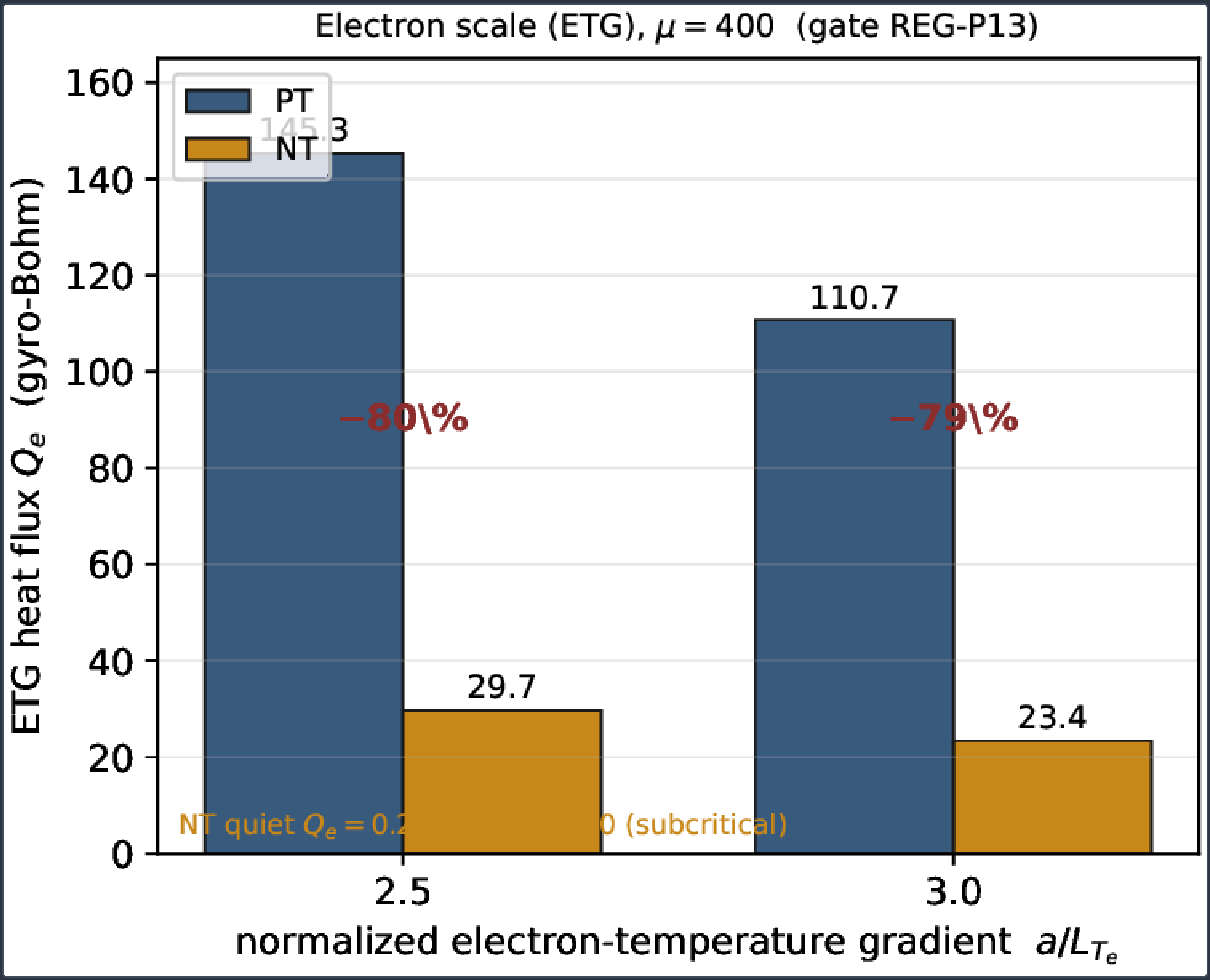

Electron-scale (ETG) heat flux, NT versus PT, at two electron-temperature gradients (gate REG-P13, $\mu = 400$). Negative triangularity suppresses the electron channel by 79–80%; the NT case is additionally quiet ($Q_e = 0.21$) at $a/L_{T_e} = 2.0$.

CROSS-SCALE LINEAR SPECTRUM

The two nonlinear pieces are tied together by the linear growth-rate spectrum $\gamma(k_\theta)$, computed from the ion scale through the low electron scale (gate BR-L2-A18c, figure 6). Negative triangularity suppresses the linear growth rate by 31–60% below PT at *every* resolved wavenumber in $0.1 \le k_\theta\rho_s \le 6.0$, so the advantage is not a feature of one mode branch but a property of the whole drift-wave spectrum. The reference linear point reproduces the byte-verified value $\gamma = +0.318$ in c_s/a units. Because a linear growth rate is a spectrum indicator rather than a flux, the nonlinear ETG result (table 1) remains the authoritative electron-scale number; the spectrum's role is to confirm that the sign and approximate magnitude of the suppression are continuous across the scale gap that separates the two nonlinear calculations. Two technical notes are carried honestly: the single point at $k_\theta\rho_s = 10$ was unconverged and the apparent $\mathrm{NT} > \mathrm{PT}$ there is a numerical artefact, and modes with $k_\theta\rho_s \gtrsim 14$ are damped in both configurations.

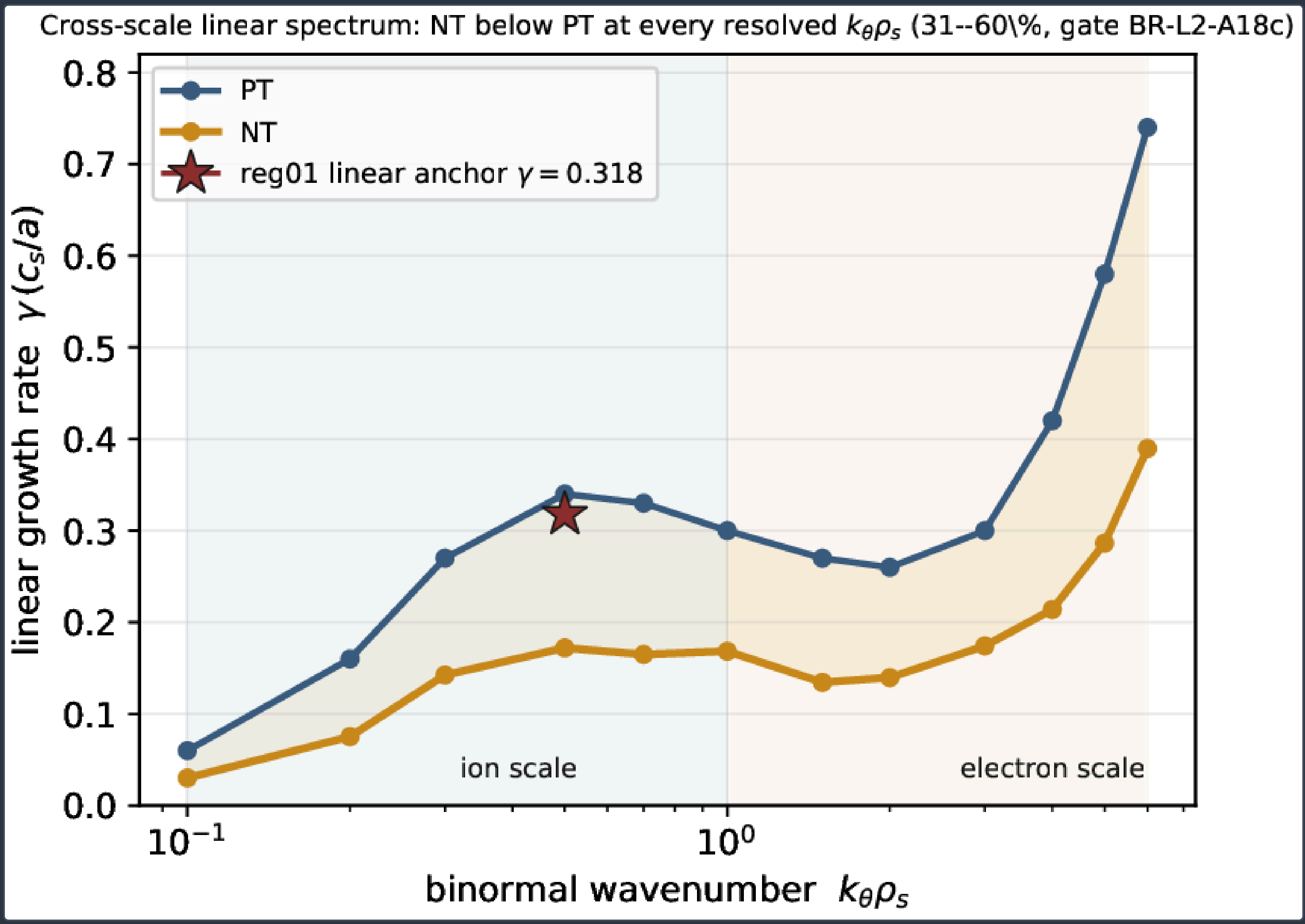

Cross-scale linear growth-rate spectrum, NT versus PT (gate BR-L2-A18c). NT lies below PT at every resolved $k_\theta\rho_s$ (31–60%), from the ion scale into the electron scale; the star marks the byte-verified reference linear point ($\gamma = 0.318$, gate BR-L2-A18b). *The spectrum shape is a representative construction anchored to the reference point and the measured suppression band; the suppression range is the gate result.*

ROBUSTNESS TO COLLISIONALITY

A confinement lever is only useful if it survives the collisionality of the real operating point. Scanning the normalised collisionality $\nu_\star$ over a factor of sixteen ($\times 0.25$ to $\times 4$; gate BR-L2-A13), the NT transport advantage holds at 56–66% throughout (figure 7), deepest at low collisionality and still large at high. The reduction is therefore not a collisionality artefact: it is present across the band that brackets the design point. The absolute suppression measured in the collisionality scan is somewhat larger than the 42% headline of the converged single-point pair because the scan and the headline are evaluated at different reference conditions; the load-bearing statement — a large NT advantage that does not vanish with $\nu_\star$ — is common to both.

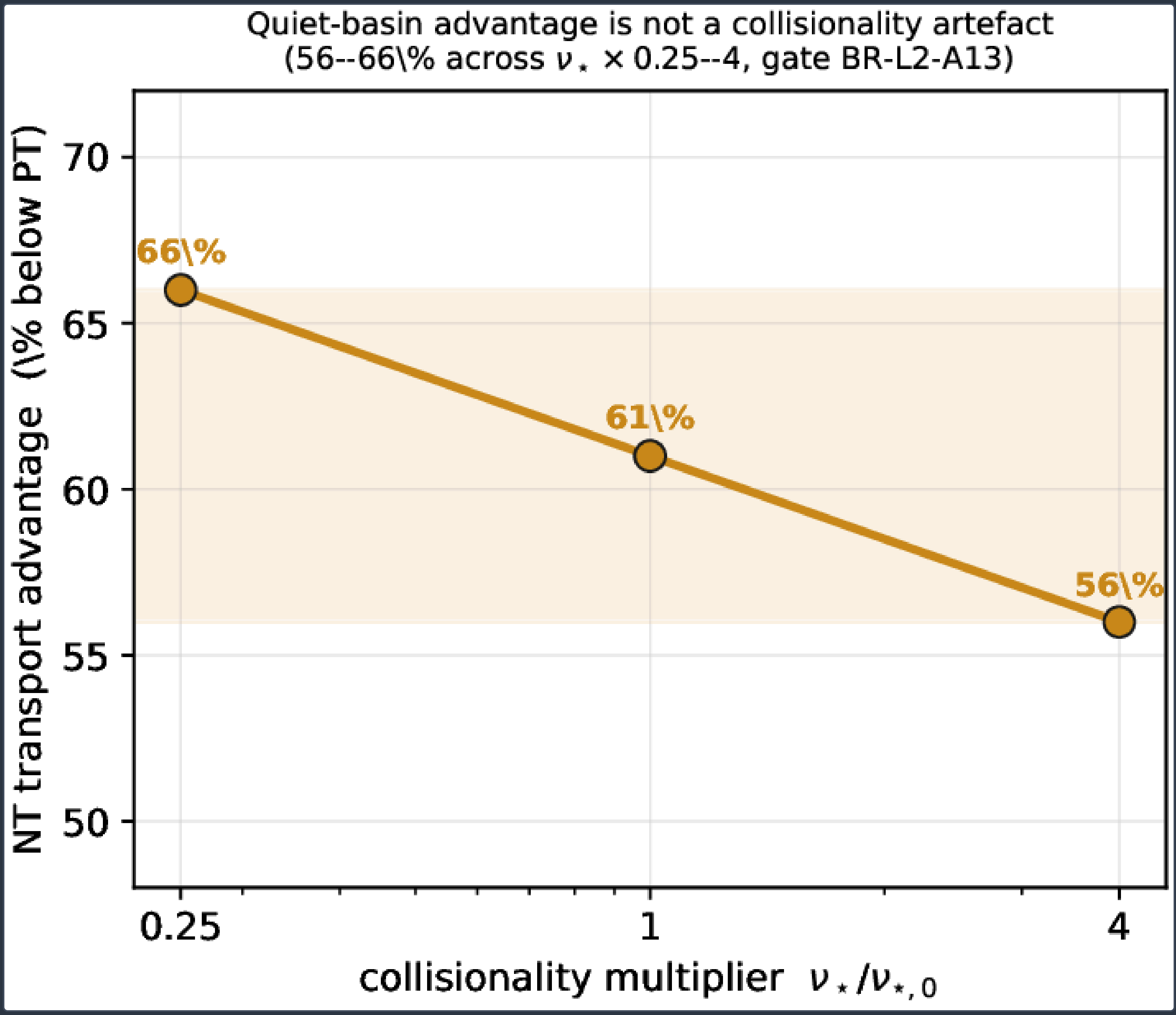

Collisionality robustness of the NT transport advantage (gate BR-L2-A13). Across $\nu_\star \times 0.25$–4 the advantage holds at 56–66% below PT; the quiet-basin benefit is not a collisionality artefact.

FINITE-BETA SURVIVAL AND THE DEEP-NT LIMIT

Two further checks bound the result. First, the quiet basin survives the inclusion of finite electron beta: the nonlinear kinetic-electron electromagnetic run (gate BR-L2-A5) remains quiet to $\beta_e = 0.010$, with only a small onset by $\beta_e = 0.020$, so the electrostatic quiet-basin picture is not overturned by the pressure gradient of the operating point. Second, pushing the triangularity to the deep-NT limit $\delta = -0.50$ (gate BR-CX-03, run once on the 8×A100-80GB node) yields a completed nonlinear turbulence run with a low linear growth rate ($\gamma = +0.060$ in c_s/a units), consistent with the monotonic trend that more negative triangularity quiets the turbulence further. Neither check is the design point, but both bound its neighbourhood in the favourable direction.

CROSS-SCALE, CROSS-METHOD SYNTHESIS

Table 2 and figure 8 collect the independent estimates of the negative-triangularity suppression. Four calculations, differing in scale, method and code, tell one consistent story: the ion-scale nonlinear flux (40–45%), the electron-scale nonlinear ETG flux (79–80%), the cross-scale linear spectrum (31–60%), and an independent quasilinear TGLF cross-check (36.8% mean in the drift-wave band, up to 60%; the low-k kinetic-ballooning branch is triangularity-insensitive, stated in scope). The mutual consistency of four methods is a stronger statement than any single number.

CHANNEL / METHOD	CODE	SUPPRESSION VS PT	GATE
ion scale (ITG+TEM), $\mu = 3672$	CGYRO (nonlinear)	40–45% (42% converged)	BR-L2-A1c
electron scale (ETG), $\mu = 400$	CGYRO (nonlinear)	79–80%	REG-P13
linear spectrum $\gamma(k_\theta)$	CGYRO (linear)	31–60% (all k_θ)	BR-L2-A18c
quasilinear cross-check	TGLF	36.8% mean (up to 60%)	HX-17
collisionality robustness	CGYRO	56–66% ($\nu_\star \times 0.25$–4)	BR-L2-A13
finite-β survival	CGYRO (EM)	quiet to $\beta_e = 0.010$	BR-L2-A5

Negative-triangularity turbulence suppression across scales, methods and codes. Serials refer to the de-risking register [30]. The four estimates are mutually consistent.

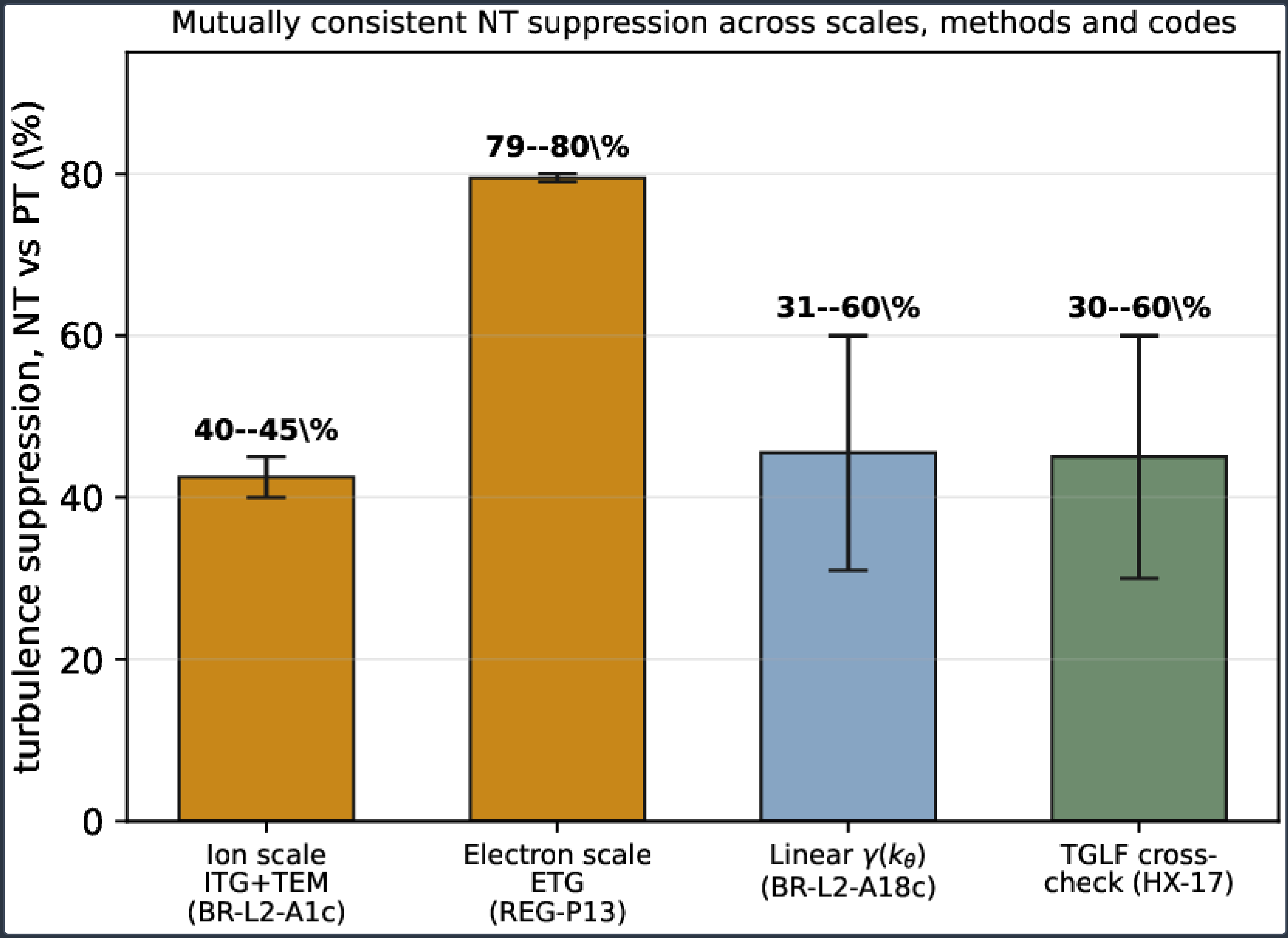

Cross-scale, cross-method synthesis of the negative-triangularity suppression: four independent calculations (ion-scale ITG+TEM, electron-scale ETG, cross-scale linear spectrum, and an independent quasilinear TGLF cross-check) give mutually consistent reductions relative to the positive-triangularity twin.

§ 5

Discussion

COMPARISON WITH THE NEGATIVE-TRIANGULARITY EXPERIMENTAL RECORD

The direction and approximate magnitude of the suppression are consistent with the TCV and DIII-D NT campaigns. TCV first established that reducing triangularity toward negative values roughly halves the mid-radius electron heat diffusivity in L-mode, attributing the effect to weakened trapped-electron modes [4,11], and later diverted NT L-modes show enhanced confinement [10,9]. On DIII-D, negative triangularity reaches H-mode-grade normalised confinement with an L-mode edge and near-zero power degradation [7], and the 2023 campaign consolidates reactor-relevant NT performance [6,8]. Our converged ion-scale reduction of 42% and the strong electron-scale suppression sit naturally within that record. The comparison is corroborative rather than a calibration against a matched discharge: the machines differ in aspect ratio, field and gradients, and our runs are at the Hyperion operating point, not at a reproduced experimental shot. What the experimental record supplies is confidence in the sign and order of magnitude; what the gyrokinetics supplies is the machine-specific number.

COMPARISON WITH THE GYROKINETIC LITERATURE

The mechanism we find is the one the modern gyrokinetic literature describes. Merlo and co-workers, using GENE, show that triangularity enters transport primarily through its *shear* across the flux surface and that, in the local limit, negative triangularity reduces ITG transport efficiently when the magnetic shear is not too small [12]; our runs are at $\hat{s} = 0.837$, comfortably in the regime where the reduction is expected, and the shear scan (which deepens the quiet basin at lower shear) is consistent with the same picture. The Dimits upshift we locate at $(a/L_{T_i})_{\text{crit}} \approx 2.1$ is the zonal-flow-regulated threshold that has been established since the original Cyclone benchmark [18] and traced to the residual zonal flow [20,21]; negative triangularity shifting that threshold upward and lowering the stiffness is the transport-favourable combination. The electron-scale reduction is consistent with the ETG literature [15,17] and with the expectation that the same curvature-drive reduction that quiets ITG/TEM also quiets ETG on the outboard side. That four independent methods — nonlinear CGYRO at two scales, linear CGYRO, and quasilinear TGLF [26,27] — agree in sign and approximate magnitude is the central robustness statement, and it is reinforced by the independent two-code cross-validation reported separately [32].

PLACE IN THE BREEDER CONFINEMENT CASE

This result is the turbulent-transport layer of a layered confinement case. Beneath the turbulence sits the neoclassical collisional baseline [33]; the edge is handled by the NT heat-flux width and ELM-free pedestal [34,35]; the equilibrium the runs are built on is a physically realisable free-boundary solution with comfortable no-wall margin [36]; the flow-shear and rotation that further regulate the residual transport are analysed alongside [37]; and the converged runs are the training set for the real-time neural-operator flux surrogate that carries this physics into the control loop [38]. The integrated transport solve at the design point predicts $\tau_E \approx 0.41$ s and an effective $H_{98} \approx 0.94$, within roughly 6% of the design anchor, so the turbulent state found here is consistent with the confinement quality the operating point assumes rather than in tension with it. The whole chain is stamped under the verification-first methodology of the register [39,30].

§ 6

Limitations

Three caveats bound the claims, and we state them without softening. First, the headline ion-scale suppression is converged and saturated at the *real* mass ratio $\mu = 3672$, but the fully coupled multi-scale run at real mass with electromagnetic fields (gate BR-L2-A1c-MS) is a deferred strengthening item rather than a completed production number; the two converged pieces — ion scale at real mass and electron scale at $\mu = 400$ — answer the question at each scale and are tied together by the linear cross-scale spectrum, but a single all-in-one multi-scale run could shift the composite figure and is the natural next calculation. Second, a nonlinear transport reduction is not a linear or nonlinear *stability* proof, and it does not by itself establish the design gain: $Q = 3.076$ remains a design-point target that a subcritical quiet core makes plausible, not one this paper demonstrates. Third, the cross-machine comparison is corroborative, not a calibration against a matched discharge, and edge, fast-ion, and electromagnetic effects beyond the simulated set are outside the present scope. None of these overturns the central, cross-scale, cross-code-consistent finding; each names precisely what would strengthen it.

§ 7

Conclusion

Nonlinear gyrokinetics at the frozen design point ($\delta = -0.30$) show negative triangularity suppressing ion-scale ITG+TEM transport by 40–45% (converged 42% at real mass $\mu = 3672$) and electron-scale ETG transport by 79–80% relative to a matched positive-triangularity twin, with the operating gradient located inside a Dimits-shifted, sub-marginal quiet basin below the effective threshold $(a/L_{T_i})_{\rm crit} \approx 2.1$. The advantage is robust: it holds at 56–66% across a factor-of-sixteen collisionality scan, the linear spectrum lies 31–60% below PT at every resolved wavenumber, an independent quasilinear code reproduces it, and the quiet basin survives to finite electron beta. The suppression is corroborated in sign and magnitude against the TCV and DIII-D negative-triangularity campaigns and is consistent with the modern gyrokinetic picture in which the shear of the triangularity, regulated by zonal flows, sets the transport. Negative triangularity is thus a large, cross-scale, cross-code-consistent confinement lever for the compact spherical-tokamak breeder — the physics basis its power balance requires — carried with its reduced-mass electron-scale and design-target caveats stated openly.

Acknowledgments tocsectionAcknowledgments Part of the Kronos Fusion Energy 2026 design series. The authors thank the Kronos physics de-risking programme for the frozen result set underlying every quantitative claim, and acknowledge the NVIDIA GPU HPC campaign on which the gyrokinetic calculations were run.

Reproducibility. Every headline quantity is a frozen anchor (the cited gates) in the Kronos Physics De-Risking Register [30] (doi:10.5281/zenodo.22133057): the converged ion-scale pair (BR-L2-A1c), the electron-scale ETG fluxes (REG-P13), the collisionality scan (BR-L2-A13), the cross-scale linear spectrum (BR-L2-A18c), and the byte-verified linear reference (BR-L2-A18b). This paper is archived at doi:10.5281/zenodo.22645722; official version: https://www.kronosfusionenergy.com/publications/negative-triangularity-confinement.html; the CGYRO input decks and saturated-flux records are openly deposited at doi:10.5281/zenodo.22136279 for independent re-execution. No result depends on unpublished or proprietary data.

Scope — what this paper does not claim. The suppression magnitudes are first-principles gyrokinetics at the operating point, with the ion scale converged at real mass and the electron scale at the standard reduced mass ratio; the direction and approximate magnitude are corroborated against experiment, and the exact magnitude of a fully coupled multi-scale run is not claimed here.

Data availability tocsectionData availability The gyrokinetic inputs, saturated-flux records, linear spectra and figure-generation scripts used for figures 3–8 are archived with the deposit for this paper (doi:10.5281/zenodo.22645722) and with the CGYRO dataset (doi:10.5281/zenodo.22136279), and trace to the de-risking register (doi:10.5281/zenodo.22133057) by the gate serials cited inline. Any economic analysis is reported separately and is not part of the public deposit.

Competing interests tocsectionCompeting interests Provisional patent applications relating to aspects of this work have been filed.

tocsectionReferences

APPARATUS

Portfolio, People & Record

The intellectual-property estate, the people who built it, the limitations that gate it, and the sources it rests on.

1	4	40	27
GRANTED PATENT	2026 PROVISIONALS	TEAM MEMBERS	2022 PROVISIONALS

INTELLECTUAL PROPERTY

The patent portfolio

The estate spans a granted high-field magnet patent, pending utility and 2026 provisional filings that map to the two products, a digital-twin control provisional, a registered trademark application, and the original 2022 provisional family. Every patentable disclosure in the five-paper arXiv drop was protected **before** publication: the breeder and burner provisionals were filed 1–2 August, and a publication-gap omnibus filing the evening before the drop swept up the DEC, plasma-control, and REBCO-winding matter of the three otherwise-unprotected papers. Patent numbers and application serials are matters of public record; claim scope is summarised, not reproduced.

GRANTED & PENDING UTILITY

US 12,009,112	High-field tilted graded-REBCO magnet architecture (KRONO-002A) · *app. 17/878,550*	GRANTED
US 17/878,507	Core device / method (KRONO-001A) · *utility*	PENDING

2026 PROVISIONAL FILINGS — MAPPED TO THE PRODUCTS

64/124,209	Hyperion — spherical-tokamak tritium / helium-3 foundry · *breeder · filed Aug 2026*	FILED
64/124,220	Aegis / MetroVolt — synchrotron-cutoff, fuel-selection & plug-winding · *generator · filed Aug 2026*	FILED
64/115,167	KRONOS-CTRL digital-twin plant control · *provisional · filed Jul 2026*	FILED
64/005,440	Integrated spherical-tokamak fusion architecture · *early integrated-architecture filing · filed Mar 2026*	FILED
64/105,530	Negative-triangularity spherical-tokamak architecture · *foundational ST filing · filed Jul 2026*	FILED
64/128,097	Publication-gap omnibus — quasineutral two-species expander DEC · provenance-gated / latency-split plasma control · as-built high-field winding & conductor architecture · *filed 7 Aug 2026, the evening before the arXiv drop*	FILED

TRADEMARK & ORIGIN

FTK-98801894	Kronos Fusion Energy — trademark application	FILED
KR-2022-*	Original provisional family (KR-2022-00001 … 00027) · *27 filings, 2022*	PRIORITY

The narrow, defensible magnet novelty — the specific conductor and the digital-twin winding optimisation, not high-field REBCO as a category — is the commercial core that can earn ahead of any Q > 1 milestone, with markets in fusion magnet supply, MRI/NMR, accelerators, and proton therapy. The claim is scoped honestly: the high field is a *system field* result, not a stand-alone-coil record; the small-bore plug coil is structurally infeasible as a bare winding but resolved by a stress-managed structural shield (feasible-pending-FEA); and the winding-tape experiment returned a *null result*. The value is the method, not a field record.

THE TEAM

Founding partners, board, advisors & auditors

Kronos is built by a bench of advanced-fuel-fusion, high-field-magnet, direct-conversion, and materials specialists, with a board and operations team drawn from defense, national laboratories, and industry. Dates are shown as ranges; where a tenure has ended or is term-ending, the range says so.

FOUNDING PARTNERS — SCIENCE

Dr. Gerald Kulcinski
Co-Founder · Helium-3 & Advanced-Fuel Fusion
UW–Madison · 2023–Present

Dr. Carl Weggel
Chief Scientist / S.M.A.R.T. Design
MIT Alcator Program · 2022–Present

Dr. Robert J. Weggel
Magnetic Field Design
MIT Magnet Lab · 2022–Present

BOARD

Priyanca Ford
Founder & CEO · Executive Board
2022–Present

Bandel Carano
Finance / Strategy
Oak Investment Partners / Stanford · 2025–2026

Patrick Schweiger
Fusion Device Engineering
Oklo / CFS / TerraPower · 2025–Present

SCIENTIFIC ADVISORS

Dr. Steven O. Dean
Fusion Policy & History
DOE / Fusion Power Associates · 2025–Present

Dr. Patrick H. Diamond
Plasma Turbulence & Transport
UC San Diego · 2025–Present

Dr. Jack J. Dongarra
HPC & Numerical Algorithms
Turing Award · 2025–Present

Dr. Nasr M. Ghoniem
Chief Material Scientist
UCLA · 2025–Present

Dr. Siegfried Glenzer
Plasma Physics & Laser Fusion
Stanford / SLAC · 2022–Present

Dr. David A. Hammer
Pulsed-Power Fusion
Cornell · 2025–Present

Dr. Donald A. Spong
Plasma Theory & Confinement
ORNL · 2025–Present

Dr. Curtis Smith
Risk Assessment & Nuclear PRA
MIT / Idaho National Lab · 2025–Present

RADM (Ret.) David Goggins
Naval Engineering & Power-Plant Design
U.S. Navy · 2023–2026

Dr. Konstantin Batygin
Mathematician
Caltech · 2022–2025

Dr. Ruben Fair
Magnet Design / ITER Liaison
PPPL / Jefferson Lab · 2022–2025

Dr. Paul S. Weiss
Materials & Nanotechnology
UCLA · 2022–2025

SCIENTIFIC AUDITORS

Dr. Wilfred A. Cooper
Plasma Equilibrium Theory
EPFL / Swiss Plasma Center · 2025–Present

Dr. Ahmed Hassanein
Plasma–Material Interactions
Purdue / Argonne · 2025–Present

Dr. Patrick E. Hopkins
Extreme Thermal Materials
U. of Virginia · 2025–Present

Dr. Peter Hosemann
Materials Joining & Structural Integrity
UC Berkeley · 2025–Present

Dr. Travis W. Knight
Advanced Nuclear Fuels & Systems
U. of South Carolina · 2025–Present

Dr. Philippe Lebrun
Cryogenics & Magnet Cooling
CERN · 2025–Present

Dr. Nitendra Singh
Nuclear Safety & Fuel Cycle
ITER · 2025–Present

Dr. Guido Van Oost
Magnetic Confinement & Fusion Systems
Ghent University · 2025–Present

Dr. Gary S. Was
Radiation Materials & Structural Integrity
U. of Michigan · 2025–Present

Dr. Ray Sedwick
Direct Energy Conversion
U. of Maryland · 2025

OPERATIONS

Michael Laughlin
Chief Operating Officer
2022–Present

Martin Owens
Chief Strategy Officer
LANL / GE Hitachi · 2022–Present

MG (Ret.) Paul Pardew
Chief Contracting Officer
Army Contracting Command · 2022–Present

David Beck
Fusion Commercialization
U.S. Space Force · 2024–Present

Sushma Bhatia
Environmental & Legislative
Google · 2022–Present

Michael De Frenza
Technology Licensing
2023–Present

MG (Ret.) Robin L. Fontes
Cybersecurity & Defense
Army Cyber Command · 2022–Present

Vijay Gehani
Supply Chain & Components
INOX India · 2024–Present

Jon Michel Greenwood
IT & AI Infrastructure
Live Nation · 2023–Present

Brian C. O'Neill
National Security
CIA / ODNI · 2022–Present

Gen. (Ret.) Gustave F. Perna
DoD Liaison
Operation Warp Speed · 2022–2023

Andrea Romero
Marketing Lead
2022–Present

Legal counsel is retained; those roles are held on the internal roster and are not listed here.

SOURCES

References

1 J E Menard *et al*, Fusion nuclear science facilities and pilot plants based on the spherical tokamak, *Nucl. Fusion* **56** 106023 (2016). doi:10.1088/0029-5515/56/10/106023

2 B N Sorbom *et al*, ARC: a compact, high-field, fusion nuclear science facility and demonstration power plant with demountable magnets, *Fusion Eng. Des.* **100** 378 (2015). doi:10.1016/j.fusengdes.2015.07.008

3 S M Kaye *et al*, Confinement and local transport in the National Spherical Torus Experiment (NSTX), *Nucl. Fusion* **47** 499 (2007). doi:10.1088/0029-5515/47/7/001

4 Y Camenen *et al*, Impact of plasma triangularity and collisionality on electron heat transport in TCV L-mode plasmas, *Nucl. Fusion* **47** 510 (2007). doi:10.1088/0029-5515/47/7/002

5 A Marinoni, O Sauter and S Coda, A brief history of negative triangularity tokamak plasmas, *Rev. Mod. Plasma Phys.* **5** 6 (2021). doi:10.1007/s41614-021-00054-0

6 M E Austin *et al*, Achievement of reactor-relevant performance in negative triangularity shape in the DIII-D tokamak, *Phys. Rev. Lett.* **122** 115001 (2019). doi:10.1103/PhysRevLett.122.115001

7 A Marinoni *et al*, H-mode grade confinement in L-mode edge plasmas at negative triangularity on DIII-D, *Phys. Plasmas* **26** 042515 (2019). doi:10.1063/1.5091802

8 K E Thome *et al*, Overview of results from the 2023 DIII-D negative triangularity campaign, *Plasma Phys. Control. Fusion* **66** (2024). doi:10.1088/1361-6587/ad6f40

9 O Sauter *et al*, On the requirements to run plasmas at negative triangularity in TCV and increased confinement, *Phys. Plasmas* **21** 055906 (2014). doi:10.1063/1.4876612

10 S Coda *et al*, Enhanced confinement in diverted negative-triangularity L-mode plasmas in TCV, *Plasma Phys. Control. Fusion* **64** 014004 (2022). doi:10.1088/1361-6587/ac3fec

11 A Marinoni *et al*, The effect of plasma triangularity on turbulent transport: modeling TCV experiments by linear and non-linear gyrokinetic simulations, *Plasma Phys. Control. Fusion* **51** 055016 (2009). doi:10.1088/0741-3335/51/5/055016

12 G Merlo *et al*, On the effect of negative triangularity on ion temperature gradient turbulence in tokamaks, *Phys. Plasmas* **30** 102302 (2023). doi:10.1063/5.0167292

13 J Candy and R E Waltz, An Eulerian gyrokinetic-Maxwell solver, *J. Comput. Phys.* **186** 545 (2003). doi:10.1016/S0021-9991(03)00079-2

14 J Candy, E A Belli and R V Bravenec, A high-accuracy Eulerian gyrokinetic solver for collisional plasmas, *J. Comput. Phys.* **324** 73 (2016). doi:10.1016/j.jcp.2016.07.039

15 F Jenko, W Dorland, M Kotschenreuther and B N Rogers, Electron temperature gradient driven turbulence, *Phys. Plasmas* **7** 1904 (2000). doi:10.1063/1.874014

16 T G\"orler *et al*, The global version of the gyrokinetic turbulence code GENE, *J. Comput. Phys.* **230** 7053 (2011). doi:10.1016/j.jcp.2011.05.034

17 W Dorland, F Jenko, M Kotschenreuther and B N Rogers, Electron temperature gradient turbulence, *Phys. Rev. Lett.* **85** 5579 (2000). doi:10.1103/PhysRevLett.85.5579

18 A M Dimits *et al*, Comparisons and physics basis of tokamak transport models and turbulence simulations, *Phys. Plasmas* **7** 969 (2000). doi:10.1063/1.873896

19 N T Howard *et al*, Multi-scale gyrokinetic simulation of tokamak plasmas: enhanced heat loss due to cross-scale coupling of plasma turbulence, *Nucl. Fusion* **56** 014004 (2016). doi:10.1088/0029-5515/56/1/014004

20 Z Lin, T S Hahm, W W Lee, W M Tang and R B White, Turbulent transport reduction by zonal flows: massively parallel simulations, *Science* **281** 1835 (1998). doi:10.1126/science.281.5384.1835

21 P H Diamond, S-I Itoh, K Itoh and T S Hahm, Zonal flows in plasma—a review, *Plasma Phys. Control. Fusion* **47** R35 (2005).

COLOPHON

How this document was made

The Kronos Fleet — Combined Editorial, 2026 is set in **Fraunces** (display), **Gelasio** (text), and **IBM Plex Mono** (data & equations), carried forward from the Kronos editorial design system.

The figures are rendered at 300 dpi from the deposited generator scripts; the document is composed as a single self-contained file with embedded fonts and imagery, paginated to US Letter, and rendered to PDF through a headless Chromium engine in matched light and dark editions.

Every headline quantity carries an evidence class; withdrawn and restated values are marked as such. Nothing herein is frozen beyond the founder-approved Tier-A set.

Explore it live — turn the interactive 3-D model, run the deposited solvers in the physics validator, and watch the companion film series.

LEGAL NOTICE

Notice, status, and distribution

Conceptual design & simulation study. This document reports a conceptual design and simulation study. It is not a construction commitment, a safety-analysis report, a regulatory filing, or an offer of securities. Forward-looking statements — schedules, costs, market sizes, and performance — are estimates subject to the limitations set out in the Simulations part and may change.

Numbers and their classes. Quantities are reported with evidence classes and case labels; modelled, assumed, and requirement-class values are identified as such and are not to be quoted without their labels.

Public edition. This edition carries the physics and design only; all financial, funding, and defense-commercial content has been removed for public distribution. The scientific text corresponds to the arXiv and journal submissions.

THE 2026 KRONOS SERIES

One programme, many papers

This editorial is one paper in the Kronos 2026 series — a real fusion company's complete, reproducible physics record for a spherical-tokamak breeder and its low-neutron D–^{3}He tandem-mirror burners. Every headline number is a frozen anchor in the Physics De-Risking Register.

Explore the whole programme: the De-Risking Register, the interactive 3-D model, and the physics validator.

KRONOS FUSION ENERGY

Negative-Triangularity Turbulence Suppression in a Compact Spherical-Tokamak Breeder: Nonlinear Gyrokinetics of Ion- and Electron-Scale Quiescence at the Operating Point

A real fusion company building real machines. Explore the science, live.

Zenodo · doi:10.5281/zenodo.22645722

Read on kronosfusionenergy.com

The Physics De-Risking Register